Am J Nucl Med Mol Imaging 2026;16(2):114-124
www.ajnmmi.us /ISSN:2160-8407/ajnmmi0169194

Original Article

Role of FDG-PET/CT in detecting metabolic changes in parotid glands following photon versus proton therapy

Om H Gandhi[1], Jaskeerat Gujral[1], Amir Amanullah[1], Miraziz Ismoilov[1], Shashi B Singh[1], Shiv Patil[1], Malia Ahmed[1], Saira K Niazi[1], Niloofaralsadat Motamedi[1], Bimash B Shrestha[1], Thomas J Werner[1], Mona-Elisabeth Revheim[2,3], Abass Alavi[1]

[1]Department of Radiology, Hospital of The University of Pennsylvania, 3400 Spruce Street, Philadelphia, PA 19104, USA; [2]The Intervention Center, Division for Technology and Innovation, Oslo University Hospital, 0424 Oslo, Norway; [3]Institute of Clinical Medicine, Faculty of Medicine, University of Oslo, 0313 Oslo, Norway

Received October 8, 2025; Accepted April 19, 2026; Epub April 25, 2026; Published April 30, 2026

Abstract: Xerostomia is a disabling side-effect of head and neck cancer (HNC) radiation therapy (RT) that significantly impacts quality of life. While proton therapy offers dosimetric advantages over photon therapy, metabolic evidence of tissue-sparing effects remains limited. This retrospective study assessed ^{18}F-FDG PET/CT for evaluating radiation-induced metabolic changes in parotid glands following proton versus photon RT in 50 HNC patients with base-of-tongue tumors treated with photon (n=14, intensity-modulated radiation therapy (IMRT)) or proton (n=36, pencil-beam scanning intensity-modulated proton therapy (IMPT)) with concurrent chemotherapy. All patients received ^{18}F-FDG PET/CT before and approximately 3 months post-treatment. Bilateral parotid glands were manually delineated and averaged per patient. Both groups demonstrated significant total mean standardized uptake value (SUV_{mean}) increases (photon: 1.13±0.23 to 1.45±0.38, P<0.001; proton: 1.30±0.27 to 1.41±0.21, P=0.017), with significantly greater increases in the photon group for both ΔSUV_{mean} (0.32 vs. 0.11, P=0.017) and ΔSUV_{max} (0.44 vs. 0.07, P=0.011; Mann-Whitney U tests). Between-group effect sizes were large (Cohen's d=0.86 and 0.95, respectively), and multivariable regression confirmed the treatment group effect (ΔSUV_{mean} β=-0.25, P=0.017, adjusting for baseline SUV and disease stage; ΔSUV_{max} β=-0.30, P=0.015, adjusting for baseline SUV). These findings suggest that proton therapy produces significantly lower increases in parotid gland ^{18}F-FDG uptake compared to photon therapy, supporting ^{18}F-FDG PET/CT as a quantitative biomarker for radiation-induced parotid gland injury. Future prospective studies correlating metabolic changes with functional outcomes are warranted.

Keywords: ^{18}F-FDG PET/CT, head and neck cancer, parotid gland, photon therapy, proton therapy, radiation-induced toxicity, radiation therapy, xerostomia

Introduction

Head and neck cancers (HNC) are the seventh most common malignancy worldwide, arising from the oral cavity, oropharynx, nasopharynx, hypopharynx, larynx, nasal cavity, and major salivary glands. In 2016, HNC accounted for 4 million prevalent cases, 1 million new diagnoses, and 500,000 deaths globally, with an average age at diagnosis of 60 years [1]. ^{18}F-fluorodeoxyglucose positron emission tomography/computed tomography (^{18}F-FDG PET/CT) outperforms both CT and magnetic resonance imaging (MRI) for detecting local nodal metastases, distant metastases, and secondary primary tumors [2]. HNC management depends on primary tumor location, disease stage, and tumor resectability; early-stage cancers are typically treated with surgery or radiation therapy (RT), while locally advanced tumors receive RT combined with chemotherapy [3].

Photon RT, a primary treatment modality for HNC, delivers ionizing radiation where energy deposition is spread along the entire path of the beam, often damaging surrounding normal tissues and resulting in adverse effects. In contrast, proton RT offers a distinct physical advantage through its characteristic Bragg peak, where energy deposition is concentrated at a specific depth within the tumor while minimizing dose to surrounding healthy tissues [4]. This precise dose distribution reduces exit dose beyond the target volume and spares adjacent critical structures. Comparative studies have demonstrated that proton RT delivers significantly lower radiation doses to organs at risk in HNC patients compared to photon RT, protecting critical structures in anatomically complex regions [5-7].

Xerostomia, or dry mouth, is among the most frequent and debilitating toxicities of HNC RT, typically arising when the parotid and submandibular salivary glands are exposed to high radiation doses [8]. Several investigations have examined radiation dose parameters to the parotid glands as predictors of xerostomia, but these dosimetric parameters do not always correlate with clinical outcomes and fail to capture individual biological responses to radiation exposure [9-12]. ^{18}F-FDG PET/CT can provide insights into radiation-induced tissue changes by detecting metabolic alterations in organs at risk following RT, as increased tissue glucose metabolism has been shown to indicate processes such as inflammation, cellular repair, or metabolic stress [13, 14]. Trada et al. demonstrated that mid-treatment changes in parotid

https://doi.org/10.62347/PESP7804

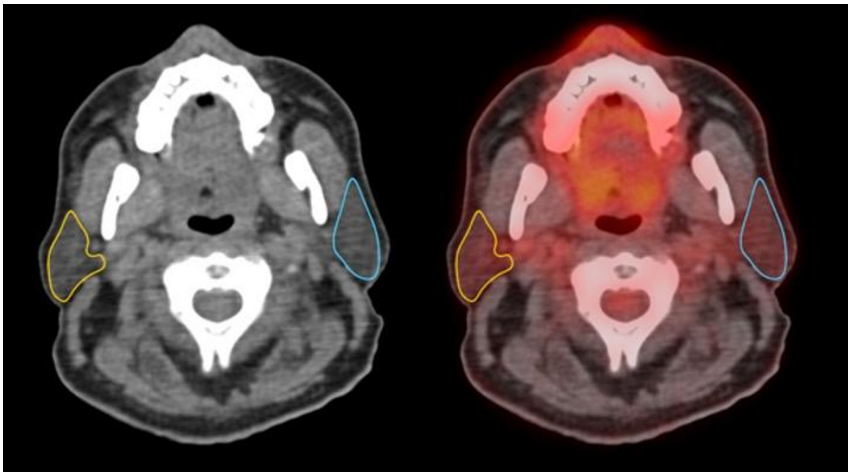

Figure 1. Example of axial ^{18}F-FDG PET/CT images with bilateral parotid gland regions of interest (outlined in blue and yellow) used for SUV quantification.

gland FDG uptake significantly correlated with subsequent moderate-to-severe xerostomia at 6 months, and that integration of PET metabolic changes with clinical factors improved xerostomia risk prediction (area under the curve [AUC] 0.777) compared to clinical factors alone (AUC 0.667) [15]. However, whether these metabolic patterns differ between photon and proton therapy modalities, and thus could inform treatment selection, remains to be established.

The aim of this study was to assess the utility of ^{18}F-FDG PET/CT in evaluating radiation-induced metabolic changes in parotid glands of HNC patients treated with photon or proton therapy. By quantifying ^{18}F-FDG uptake as a surrogate marker of tissue response, we sought to determine whether distinct metabolic patterns emerge between the two treatment approaches.

Materials and methods

Patient population

A retrospective analysis was performed with patients with HNC who had undergone either photon or proton RT along with chemotherapy. The study included patients with primary tumor located in the base of the tongue with ^{18}F-FDG PET/CT before and after RT. Patients were excluded if they had poor-quality images which prevented distinct delineation of parotid gland borders, discordance between PET and CT images, or tumor metastasis within or adjacent to the parotid gland. All patients underwent PET/CT imaging before and after photon or proton RT delivered with concurrent cetuximab or cisplatin-based chemotherapy. The mean interval between treatment and follow-up PET imaging was 90 days (range 76-102, SD: 8 days) for the photon RT group and 95 days (range 37-134, standard deviation (SD): 17 days) for the proton RT group. All patient data were anonymized. The study was conducted in compliance with Health Insurance Portability and Accountability Act (HIPAA) guidelines. This study was approved by the Institutional Review Board of the University of Pennsylvania with a waiver of informed consent due to the retrospective design and use of de-identified data. Photon RT was delivered using intensity-modulated radiation therapy (IMRT) techniques, while proton RT utilized pencil-beam scanning intensity-modulated proton therapy (IMPT). The median prescription dose was 7000 cGy (range 4400-7800 cGy) for the photon group and 6300 cGy (range 5993-11,550 cGy) for the proton group. Treatment was delivered in standard fractionation schedules with concurrent cetuximab or cisplatin-based chemotherapy.

FDG-PET/CT image acquisition & analysis

All patients fasted for a minimum of six hours prior to administration of 15 millicuries (mCi) ^{18}F-FDG radiotracer intravenously. Before administering ^{18}F-FDG, serum glucose levels were immediately measured to ensure levels were below 11 mmol/L (200 mg/dL) for accurate tracer uptake. Patients underwent PET/CT scanning approximately 60 minutes after receiving ^{18}F-FDG. The standard institutional imaging protocol was followed, and scans were obtained on hybrid PET/CT scanners with comparable spatial resolution including Philips Ingenuity TF/Gemini TF 16, Siemens 923/Biograph 64 mCT, and Philips Ingenuity TF systems. Institutional PET/CT protocol was compiled, including quality control, calibration, and cross-calibration of PET/CT scanners and validation of standardized uptake value (SUV) measurements. All PET/CT scanners were cross-calibrated to the dose calibrator. On a monthly basis, a uniform phantom was imaged on all PET/CT scanners, and the average SUVs were compared to the ideal value of 1.0. If the average SUV of a scanner differed by more than 5% from the ideal value, corrective adjustments were performed (Siemens Scanner Cross Calibration procedure for Siemens systems; lookup table value adjustment for Philips scanners). No formal image harmonization was performed across scanners; rather, reconstruction parameters were individually optimized for each system to achieve the best possible clinical image quality [16-18]. For CT scans, body mass index (BMI) under 30, BMI between 30 and 35, and BMI above 35 were acquired using CT settings of 50, 100, and 150 milliampere-seconds (mAs) at 120 kilovolt peak (kVp), respectively. The time per bed for the PET acquisitions was 1.5, 2, and 3 minutes, respectively. PET images were adjusted for scanner dead time, random coincidences, scattering, and attenuation.

OsiriX MD software version 12.5.7 was used to assign regions of interest (ROI) and measure ^{18}F-FDG uptake within the left and right parotid glands. ROIs were manually drawn around the left and right parotid glands on sequential axial PET/CT slices (**Figure 1**). The anatomical

Table 1. Anatomical boundaries used for parotid gland delineation on axial CT images during region-of-interest placement

Direction	Primary Landmarks	Secondary Landmarks	Clinical Notes
Superior	External acoustic meatus	Mastoid process of temporal bone	Upper boundary extends to level of zygomatic arch
Inferior	Posterior aspect of submandibular space	Angle of mandible	Lower boundary typically at level of hyoid bone
Anterior	Masseter muscle (superficial portion)	Posterior border of mandibular ramus; medial and lateral pterygoid muscles	Extends to posterior edge of mandibular body
Posterior	Mastoid process of temporal bone	Anterior belly of SCM; external auditory canal	Forms relationship with styloid process and carotid sheath
Medial	Styloid process and stylomandibular ligament	Posterior belly of digastric muscle; parapharyngeal space	Deep lobe extends medially around posterior border of mandible
Lateral	Subcutaneous fat layer	Platysma muscle; superficial musculo-aponeurotic system	Superficial lobe lies immediately beneath skin and platysma

SCM = sternocleidomastoid muscle.

borders of parotid glands used for ROI delineation were defined as follows (**Table 1**): superiorly by the external acoustic meatus and mastoid process, inferiorly by the posterior part of the submandibular space, anteriorly by the masseter muscle, posterior border of the mandibular bone, and medial and lateral pterygoid muscles, posteriorly by the mastoid process of the temporal bone and anterior belly of the sternocleidomastoid muscle, medially by the styloid process, posterior belly of the digastric muscle, and parapharyngeal space, and laterally by the subcutaneous fat and platysma muscle. Mean standardized uptake value (SUV_{mean}) was calculated as the average of all voxels within the defined ROI. Total SUV maximum (SUV_{max}) was determined as the average SUV_{max} from axial slices weighted according to the cross-sectional area of the ROI in each slice. For each patient, left and right parotid gland SUV values were averaged to yield a single SUV_{mean} and SUV_{max} per patient, ensuring statistical independence of observations.

Statistical analysis

For each patient, SUV_{mean} and SUV_{max} values were obtained from pre- and post-RT scans. Within-group comparisons were analyzed using two-tailed paired t-tests, with Wilcoxon signed-rank tests as non-parametric confirmation. Between-group differences in mean change (ΔSUV) were assessed with two-tailed unpaired t-tests (Welch's t-test to account for unequal variances) and confirmed with Mann-Whitney U tests. Effect sizes were quantified using Cohen's d with 95% confidence intervals (CIs). To account for potential confounders including baseline SUV values and disease stage, multivariable linear regression models were fitted with ΔSUV as the dependent variable and treatment group, baseline SUV, and stage (dichotomized as stage IV vs. stages I-III) as independent variables. Baseline demographic and clinical characteristics were compared between groups using independent t-tests for continuous variables and Fisher's exact test for categorical variables. Cumulative cross-sectional ROI area (cm^2) was used as a surrogate for parotid gland volume, and pre- to post-treatment changes were assessed. Statistical analyses were performed using R software (R Foundation for Statistical Computing, Vienna, Austria). A *p*-value less than 0.05 was considered statistically significant.

Results

Fifty patients met inclusion criteria and were analyzed for this study (**Table 2**). Baseline characteristics were generally balanced between groups. Mean age did not differ significantly (photon 66.3 vs. proton 67.7 years, P=0.54), nor did sex distribution (Fisher's exact P=1.00). Baseline parotid SUV_{mean} was lower in the photon group (1.13±0.23) than the proton group (1.30±0.27, P=0.042), whereas baseline SUV_{max} did not differ significantly (1.63±0.30 vs. 1.81±0.37, P=0.11). Disease staging differed between the two groups. The photon RT group had no patients with stage 1 or stage 2 disease, 2 patients (14%) with stage 3 disease, and 12 patients (86%) with stage 4 disease. In the proton RT group, 4 patients (11%) had stage 1 disease, 1 patient (3%) had stage 2 disease, 5 patients (14%) had stage 3 disease, and 26 patients (72%) had stage 4 disease.

Both treatment groups demonstrated statistically significant increases in parotid gland SUV_{mean} from pre-treatment to post-treatment imaging (**Table 3**; **Figure 2A**, **2B**). In the photon RT group, SUV_{mean} increased from 1.13±0.23 to 1.45±0.38 (mean change 0.32, P<0.001). In the proton RT group, SUV_{mean} increased from 1.30±0.27 to 1.41±0.21 (mean change 0.11, P=0.017). The magnitude of SUV_{mean} increase was significantly lower in the proton RT group relative to the photon RT group (0.11 vs. 0.32, P=0.011).

SUV_{max} results differed between treatment modalities (**Table 3**; **Figure 2C**, **2D**). The photon RT group demonstrated a significant increase in SUV_{max} (1.63±0.30 to 2.07±0.67, mean change 0.44, P=0.004). In contrast, the proton RT group showed no statistically significant

Table 2. Baseline patient demographic and clinical characteristics of head and neck cancer cohorts treated with proton or photon radiation therapy

Characteristic	Photon RT (n=14)	Proton RT (n=36)	*P* value	Test
Age, mean ± SD (range)	66.3±5.2 (57-76)	67.7±7.2 (57-79)	0.544	*a*
Sex, n (%)			1.000	*b*
Male	12 (86)	30 (83)		
Female	2 (14)	6 (17)		
Race, n (%)				
White	13 (93)	35 (97)		
Tumor stage, n (%)				*b*
Stage I	0 (0)	4 (11)		
Stage II	0 (0)	1 (3)		
Stage III	2 (14)	5 (14)		
Stage IV	12 (86)	26 (72)		
Baseline SUV_{mean}, mean ± SD	1.13±0.23	1.30±0.27	0.042*	*a*
Baseline SUV_{max}, mean ± SD	1.63±0.30	1.81±0.37	0.109	*a*
Baseline parotid area (cm^2), mean ± SD	162.1±76.8	126.3±66.7	0.108	*a*

Values are presented as mean ± SD (range) or n (%). RT = radiation therapy; SUV = standardized uptake value. [a]Independent samples t-test. [b]Fisher's exact test. *P<0.05.

Table 3. Parotid gland SUV changes before and after radiation therapy with within-group and between-group comparisons

Group	Metric	Pre-RT	Post-RT	ΔSUV (mean ± SD)	Paired t	Wilcoxon	95% CI of Δ	% Change
Photon (n=14)	SUV_{mean}	1.13±0.23	1.45±0.38	0.32±0.25	<0.001*	<0.001*	0.18-0.47	+28.3%
	SUV_{max}	1.63±0.30	2.07±0.67	0.44±0.47	0.004*	<0.001*	0.17-0.71	+27.0%
Proton (n=36)	SUV_{mean}	1.30±0.27	1.41±0.21	0.11±0.26	0.017*	0.013*	0.02-0.20	+8.5%
	SUV_{max}	1.81±0.37	1.88±0.30	0.07±0.36	0.250	0.187	-0.05-0.19	+3.9%
Between-Group Comparison (Δ Photon - Δ Proton)								
ΔSUV_{mean}				0.22	0.011*	0.017*	0.06-0.38	d=0.86
ΔSUV_{max}				0.37	0.015*	0.011*	0.08-0.66	d=0.95

Values are mean ± SD. ΔSUV = post-treatment minus pre-treatment value. Paired t = paired t-test (within-group). Wilcoxon = Wilcoxon signed-rank test (within-group) or Mann-Whitney U test (between-group). 95% CI = 95% confidence interval of the mean difference. Between-group *P* values from Welch's t-test (Paired t column) and Mann-Whitney U (Wilcoxon column). d = Cohen's d effect size (95% CI: SUV_{mean} 0.22-1.50; SUV_{max} 0.30-1.59). *P<0.05.

change in SUV_{max} from pre-treatment to post-treatment (1.81±0.37 to 1.88±0.30, mean change 0.07, P=0.250). When comparing the magnitude of change between groups, the proton RT group had a significantly lower increase in SUV_{max} compared to the photon RT group (0.07 vs. 0.44, P=0.015). Non-parametric analyses confirmed all primary findings: Wilcoxon signed-rank tests supported within-group SUV_{mean} increases for both photon (P< 0.001) and proton (P=0.013) groups, while Mann-Whitney U tests confirmed significant between-group differences for both ΔSUV_{mean} (U=363, P=0.017) and ΔSUV_{max} (U=370, P=0.011) (**Figure 3**). The effect size for the between-group ΔSUV_{mean} difference was large (Cohen's d=0.86, 95% CI: 0.22-1.50), as was that for ΔSUV_{max} (Cohen's d=0.95, 95% CI: 0.30-1.59). The mean difference in ΔSUV_{mean} between photon and proton groups was 0.22 (95% CI: 0.06-0.38), and the mean difference in ΔSUV_{max} was 0.37 (95% CI: 0.08-0.66). In multivariable linear regression adjusting for baseline SUV_{mean}, the treatment group effect on ΔSUV_{mean} remained notable (β=-0.14, P=0.067). When additionally adjusting for disease stage among patients with available staging data, the group effect strengthened and reached significance (β=-0.25, P=0.017) (**Table 4**). For ΔSUV_{max}, the group effect remained significant after adjusting for baseline SUV_{max} (β=-0.30, P=0.015). Parotid gland cross-sectional area decreased significantly in both groups from pre- to post-treatment: from 162.1±76.8 to 124.8±58.5 cm^2 in the photon group (P=0.011) and from 126.3±66.7 to 102.7±47.0 cm^2 in the proton group (P=0.016). Mean percentage area reduction was -16.4% for the photon group and -10.4% for the proton group. A sensitivity analysis using area-weighted SUV values yielded results consistent with the primary analysis (between-group ΔSUV_{mean} P=0.013; ΔSUV_{max} P=0.022) (**Figures 3** and **4**) (**Table 5**).

Discussion

This study demonstrates that proton RT produces significantly smaller increases in parotid gland ^{18}F-FDG uptake

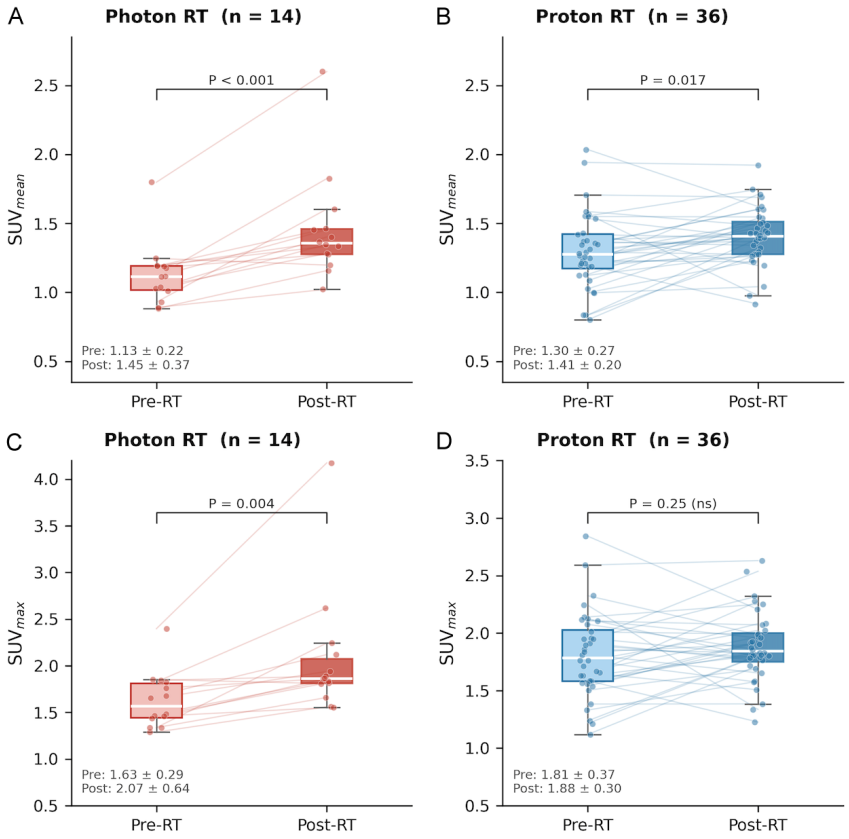

Figure 2. Box plots illustrating a comparison of parotid gland SUV_{mean} values before and after radiation therapy in patients treated with proton and photon therapy. (A) Photon RT SUV_{mean}, (B) Proton RT SUV_{mean}, (C) Photon RT SUV_{max}, (D) Proton RT SUV_{max}. Light boxes = pre-RT, dark boxes = post-RT. Individual patient trajectories shown as connecting lines. *P*-values from paired t-tests.

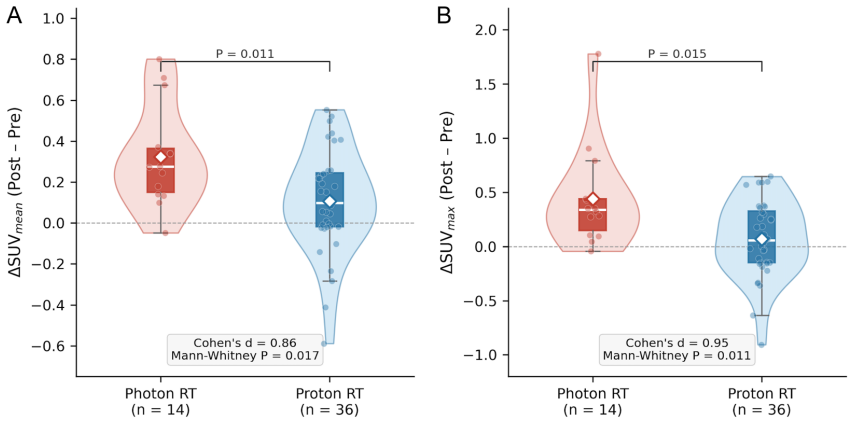

Figure 3. Box plots comparing the magnitude of parotid gland SUV changes (ΔSUV) between proton and photon treatment groups. (A) ΔSUV_{mean} and (B) ΔSUV_{max} between photon and proton groups. Violin plots show data distribution; box plots show median and interquartile range; white diamonds indicate group means. Cohen's d effect sizes and Mann-Whitney *P*-values shown.

compared to photon RT when used to treat HNC patients with tumors located at the base of the tongue. The photon therapy group exhibited substantially greater increases in SUV_{mean} and SUV_{max}, while the proton therapy group showed modest increases in SUV_{mean} with no significant change in SUV_{max}. These findings provide metabolic evidence for the dosimetric advantages of proton therapy and suggest that ^{18}F-FDG-PET/CT may serve as a quantitative biomarker for radiation-induced parotid gland injury. The difference in metabolic responses between treatment modalities reflects fundamental differences in radiation dose distribution, where proton beams deposit energy primarily at the Bragg peak within tumor tissue with minimal exit dose to surrounding healthy structures [19]. This physical advantage translates to reduced radiation exposure to parotid glands, which are radiosensitive due to their high cellular turnover rate and the vulnerability of serous acinar cells to ionizing radiation [20]. The smaller magnitude of ^{18}F-FDG uptake increase following proton therapy indicates less radiation-induced inflammation, cellular stress, and metabolic disruption in parotid tissue, supporting the clinical rationale for proton therapy in HNC where preservation of salivary function is critical.

An important consideration is the significant baseline difference in parotid SUV_{mean} between groups (photon 1.13± 0.23 vs. proton 1.30±0.27, P=0.042), which could confound between-group comparisons of ΔSUV. To address this, we performed multivariable linear regression adjusting for baseline SUV, which showed that the treatment group effect on ΔSUV_{mean} remained notable (β=-0.14, P=0.067); when additionally adjusting for disease stage, the effect reached significance (β=-0.25, P=0.017). The group effect on ΔSUV_{max} remained significant after baseline adjustment (β=-0.30, P= 0.015). Furthermore, non-parametric tests (Mann-Whitney U) confirmed all between-group differences, and large effect sizes (Cohen's d=0.86-0.95) indicate clinically meaningful separation between groups. The use of Welch's t-test to account for unequal variances between the smaller photon group and larger proton group provides additional confidence in these findings. Nevertheless, the retrospective design and modest sample size preclude definitive causal inference, and propensity score methods were not feasible given the small photon cohort.

Our results align with the study by Mouminah et al., which similarly demonstrated lower ^{18}F-FDG uptake increases in parotid glands following proton versus photon RT in

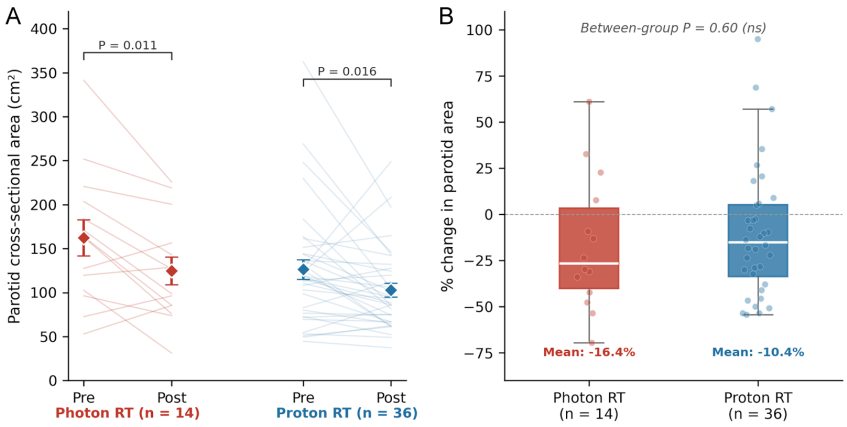

Figure 4. Parotid gland cross-sectional area changes following radiation therapy. A. Pre- and post-RT area with individual patient trajectories and mean ± SEM error bars. B. Percentage change in parotid area between groups. *P*-values from paired t-tests (within-group) and Welch's t-test (between-group).

HNC patients [21]. Our findings extend this work by examining a more homogeneous patient cohort with exclusively base-of-tongue tumors and a five-fold larger proton therapy group (n=36 vs. n=7), enabling direct statistical comparison that quantified significantly lower increases in ^{18}F-FDG uptake with proton therapy for both SUV_{mean} and SUV_{max}. However, our findings contrast with those of Roach et al., who reported dose-dependent declines in parotid gland FDG uptake following photon RT, with SUV_{mean} decreasing by approximately 5.2% per 10 Gy increase in mean parotid dose and SUV_{max} declining in a sigmoidal pattern beyond a 32 Gy threshold [22]. Several methodological differences may explain this divergent directionality. First, our study focused exclusively on base-of-tongue tumors, creating a more homogeneous population with similar radiation field configurations and dose distributions to the parotid glands, whereas Roach et al. included patients with various head and neck tumor locations across different anatomical subsites. Second, Roach et al. reported a mean post-treatment imaging time of 22 weeks (range 6-151 weeks, SD 31 weeks), with substantial variability; although the majority of their scans were obtained within 3 months, a subset extended to nearly 3 years post-treatment, and the dose-dependent decline in SUV_{mean} became more pronounced at later time points. Third, Roach et al. analyzed SUV changes as a continuous function of individual parotid mean dose using dose-volume histogram data, revealing a linear decline in SUV_{mean} of 5.2% per 10 Gy increase - an analysis that captures dose-stratified responses across individual glands rather than group-level comparisons between treatment modalities. In contrast, our study compared aggregate pre- to post-treatment SUV changes between photon and proton cohorts without individual parotid dose data, which may preferentially detect the acute inflammatory component of the radiation response rather than the dose-dependent functional decline observed at higher cumulative exposures. These differences are consistent with a biphasic metabolic response in which initial post-radiation inflammation manifests as increased ^{18}F-FDG uptake during the acute phase, followed by dose-dependent decreases as cellular damage accumulates and fibrosis or replacement of functional tissue progresses. This temporal pattern aligns with the pathophysiology of radiation-induced salivary gland damage, where acute inflammatory responses within the first few months give way to chronic changes characterized by acinar cell loss, ductal damage, and progressive fibrosis [23]. The timing of post-treatment imaging is therefore critical for interpreting metabolic changes, as measurements obtained during different phases of the radiation response may yield divergent results despite reflecting the same underlying pathophysiological process. In this study, the mean post-RT imaging interval was 90 days (range 76-102, SD 8 days) for the photon group and 95 days (range 37-134, SD 17 days) for the proton group. Because ^{18}F-FDG uptake may reflect acute inflammation at earlier time points and atrophy or fibrosis at later time points, the wider range in the proton group could influence group comparisons. Although all patients were imaged within a comparable window centered around 3 months post-treatment, future studies should standardize the post-treatment imaging interval and include timing as a covariate.

The biological mechanisms underlying increased ^{18}F-FDG uptake following RT involve specific cellular and molecular events triggered by ionizing radiation exposure. Radiation-induced DNA damage activates stress response pathways, leading to increased glucose metabolism through enhanced glycolysis, upregulation of glucose transporters, and activation of inflammatory cell populations that exhibit high metabolic activity [24-27]. Immediately following radiation exposure, damaged cells initiate repair processes that require substantial biochemical energy expenditure, which manifests as increased cellular glucose utilization detectable by ^{18}F-FDG-PET imaging. Simultaneously, radiation triggers an inflammatory response characterized by cytokine release, immune cell infiltration, and vascular changes that further contribute to elevated metabolic activity [28, 29]. In the salivary glands, radiation-induced inflammation leads to swelling, ductal obstruction, and impaired secretory activity. The associated rise in glucose metabolism is largely driven by infiltrating inflammatory cells and the activation of fibroblasts. As this process progresses, persistent inflammation results in acinar cell loss, fibrotic replacement, and subsequent decline in glandular function. The metabolic differences between photon and proton therapy groups suggest that proton therapy causes less cellular injury and inflammation. This metabolic profile is potentially consistent with better tissue preservation and may lower

Table 4. Multivariable linear regression models for ΔSUV adjusting for baseline values and disease stage

Model/Variable	β Coefficient	95% CI	*P* value	R^2	Interpretation
Model 1: ΔSUV_{mean} ~ Group + Baseline SUV_{mean} (n=50)					
Group (proton vs. photon)	-0.140	-0.290 to 0.010	0.067		Trend toward lower ΔSUV in proton
Baseline SUV_{mean}	-0.448	-0.700 to -0.196	<0.001*	0.25	Higher baseline → smaller increase
Model 2: ΔSUV_{max} ~ Group + Baseline SUV_{max} (n=50)					
Group (proton vs. photon)	-0.304	-0.546 to -0.062	0.015*		Significant proton advantage
Baseline SUV_{max}	-0.356	-0.663 to -0.049	0.024*	0.23	Regression to mean effect
Model 3: ΔSUV_{mean} ~ Group + Baseline + Stage (n=50)					
Group (proton vs. photon)	-0.253	-0.457 to -0.049	0.017*		Significant after stage adjustment
Baseline SUV_{mean}	-0.310	-0.740 to 0.120	0.151		
Stage IV (vs. I-III)	-0.087	-0.384 to 0.209	0.549	0.29	Stage not an independent predictor

β = unstandardized regression coefficient. CI = confidence interval. R^2 = model R-squared. *P<0.05.

Table 5. Parotid gland cross-sectional area changes and area-weighted SUV sensitivity analysis

Measure	Photon RT (n=14)	Proton RT (n=36)	*P* value	Test	Notes
Parotid Cross-Sectional Area					
Pre-RT area (cm^2)	162.1±76.8	126.3±66.7	0.108	t-test	
Post-RT area (cm^2)	124.8±58.5	102.7±47.0			
Δ Area (cm^2)	-37.4±47.4	-23.6±55.8			
% Area change	-16.4±36.3%	-10.4±35.2%	0.603	Welch's t	No significant group difference
Within-group change	P=0.011*	P=0.016*		Paired t	Both groups had significant shrinkage
Area-Weighted SUV Sensitivity Analysis					
Δ Weighted SUV_{mean}	0.333±0.265	0.111±0.258	0.013*	Welch's t	Consistent with primary analysis
Δ Weighted SUV_{max}	0.458±0.512	0.081±0.374	0.022*	Welch's t	Consistent with primary analysis

Values are mean ± SD. Cross-sectional ROI area (cm^2) used as a surrogate for parotid gland volume. Area-weighted SUV = Σ(SUV × area)/Σ(area) across all axial slices. *P<0.05.

the risk of chronic long-term complications such as xerostomia [30]. Consistent with this, our findings demonstrated significant parotid gland area reductions in both groups (photon: -16.4%, P=0.011; proton: -10.4%, P=0.016), alongside significantly smaller increases in SUV_{mean} in the proton group (0.11 vs. 0.32, P=0.011), supporting the hypothesis that proton therapy induces less radiation-related metabolic disruption in parotid tissue.

Several clinical studies have provided evidence that these metabolic differences translate into meaningful clinical outcomes. Blanchard et al. reported that grade ≥ 2 acute xerostomia at 3 months post-treatment occurred significantly less frequently with proton therapy compared to intensity-modulated radiation therapy (42% vs. 61%, P=0.009), while maintaining equivalent oncologic outcomes [31]. Similarly, Cao et al. observed reduced rates of xerostomia and post-treatment complications with proton versus photon therapy across multiple timepoints, and reported lasting benefits that persisted beyond 24 months after proton therapy [32]. These clinical outcomes correlate with our metabolic findings, suggesting that ^{18}F-FDG-PET/CT measurements may serve as an objective, quantitative biomarker for radiation-induced salivary gland injury that predicts subsequent functional impairment. This relationship between metabolic changes and clinical outcomes is further supported by Wilkie et al., who found a significant correlation between pre-treatment 90th percentile SUV uptake in parotid glands and the development of late xerostomia, indicating that baseline metabolic characteristics may influence susceptibility to radiation-induced damage [33]. This evidence suggests that metabolic imaging could potentially guide treatment selection, with patients at higher risk for salivary dysfunction benefiting preferentially from proton therapy or other tissue-sparing approaches.

Our observation of significant alterations in SUV_{mean} for both cohorts with SUV_{max} remaining stable in the proton group carries important implications for the use of ^{18}F-FDG PET/CT in metabolic imaging. SUV_{max} represents the highest uptake value within a single voxel and, while commonly used in oncologic imaging due to its simplicity and reproducibility, is susceptible to image noise, partial volume effects, and random fluctuations that may not reflect true biological changes [34, 35]. In contrast, SUV_{mean} incorporates all voxels within the region of interest and provides a more comprehensive assessment of overall tissue metabolism, averaging out localized variations and noise artifacts [35, 36]. When used to detect diffuse inflammatory changes following RT, SUV_{mean} offers superior sensitivity for widespread metabolic changes

affecting the entire gland, rather than focal abnormalities that might be better captured by SUV_{max}. The finding that SUV_{mean} detected significant changes in both treatment groups while SUV_{max} failed to reach significance in the proton group suggests that radiation-induced metabolic injury is broadly distributed throughout the parotid gland rather than concentrated in focal regions. This result supports using SUV_{mean} as the more reliable parameter for evaluating radiation-induced changes and indicates that whole-gland metabolic assessment offers greater clinical relevance than peak uptake measurements.

This study must be interpreted within the context of its limitations. The retrospective nature of the study, while permitting the use of available data, introduced selection bias and limits control over potential confounders that may influence metabolic measurements. The modest sample size, particularly within the photon therapy group, reduces statistical power and constrains the ability to detect subtle differences or conduct subgroup analyses. Additionally, the study's temporal framework, as analyses were confined to only two imaging time points approximately three months apart, provided an incomplete view of the dynamic response to radiation. A more informative approach would involve repeated imaging at multiple stages, beginning during treatment and continuing through both the acute recovery and chronic phases, to capture the kinetics of metabolic alterations, identify windows for predictive evaluation, and establish whether early changes forecast long-term sequelae. The absence of correlation with objective measures of salivary function, such as stimulated and unstimulated saliva flow rates, compositional analysis, or standardized xerostomia questionnaires, precluded direct validation of the clinical relevance of ^{18}F-FDG-PET/CT findings. Incorporating functional endpoints in future studies will be critical to determine whether metabolic shifts predict outcomes such as severe xerostomia, quality-of-life deterioration, or reliance on saliva substitutes. Imbalances in disease stage distribution are also noteworthy, as the photon therapy cohort included a greater proportion of stage 4 cases (86% vs. 72%), potentially biasing results given that advanced tumors often require larger radiation fields involving greater parotid gland volumes, although multivariable regression adjusting for stage confirmed the treatment group effect (P=0.017). Additionally, all patients received concurrent chemotherapy with either cetuximab or cisplatin, making it difficult to isolate the effects of RT from that of systemic therapy.

The significant reduction in parotid gland cross-sectional area observed in both groups raises the possibility that partial-volume effects may have influenced SUV measurements. Partial volume effects inherent to PET, particularly relevant in small or atrophic parotid glands, may result in underestimation of true tracer uptake [37]. However, a sensitivity analysis using area-weighted SUV values, which partially accounts for volume changes, yielded results consistent with the unweighted primary analysis, suggesting that partial-volume effects did not substantially alter our conclusions. Formal partial-volume correction was not performed and should be considered in future studies.

A limitation of our analysis is the absence of individual parotid gland dose data (mean dose and dose-volume histogram parameters), which would allow direct correlation of ΔSUV with radiation dose. The observed differences in metabolic response are attributed to the known dosimetric advantages of proton therapy; however, without patient-level parotid dose metrics, we could not definitively exclude the contribution of other factors. Future studies should incorporate detailed dosimetric data to enable dose-response analyses.

Future investigations should also consider analyzing radiation-induced metabolic changes stratified by patient-specific factors such as age and body weight, as these variables have been shown to influence tissue metabolism in other anatomical regions. Recent studies utilizing FDG-PET and NaF-PET imaging have demonstrated that gender, patient age, and weight significantly affect glucose uptake in various different joints and muscles [7, 38-42]. Similar age- and weight-related variations in baseline parotid gland metabolism may modulate the magnitude of radiation-induced metabolic changes and influence individual susceptibility to radiation-induced salivary gland injury. Incorporating these demographic variables into future analyses could refine risk stratification models and improve prediction of treatment-related toxicity [43].

The implications of these findings extend beyond comparing treatment modalities, pointing towards broader applications in personalized radiation planning and toxicity surveillance. If confirmed in larger prospective studies, ^{18}F-FDG-PET/CT could inform treatment selection by identifying patients at greatest risk for salivary dysfunction, thereby guiding the use of proton therapy or other advanced techniques, such as intensity-modulated RT as given in this study, with strict parotid constraints. Baseline metabolic imaging may also identify individuals with pre-existing parotid abnormalities or heightened radiosensitivity who require additional protective measures. Serial imaging during therapy could enable adaptive therapy modification based on early metabolic evidence of injury, while post-treatment imaging may guide early supportive care for xerostomia prevention and management [15]. Nevertheless, clinical adoption of metabolic imaging for toxicity assessment faces challenges, including the need for protocol standardization, validation across standardized post-treatment time points (e.g., approximately 3 months post-RT, as in the current study) of predictive thresholds, demonstration of cost-effectiveness, and integration into existing clinical practice. It should be

noted that ^{18}F-FDG PET/CT is already established in most clinical guidelines for HNC as a standard imaging modality at baseline staging and during follow-up when recurrence is suspected, which may facilitate its expanded use for toxicity monitoring without requiring additional imaging studies beyond those already recommended for oncologic surveillance [44, 45]. Moreover, the cumulative radiation exposure from repeated PET/CT scans, though modest, also warrants consideration, particularly in younger patients and those with favorable prognoses requiring prolonged follow-up [46].

Conclusion

This study demonstrates that proton RT produces significantly smaller increases in parotid gland ^{18}F-FDG uptake compared to photon RT in HNC patients with base-of-tongue tumors. Between-group differences were large in magnitude (Cohen's d=0.86-0.95) and robust to adjustment for baseline SUV values and disease stage in multivariable regression. Non-parametric analyses confirmed all primary findings, and a sensitivity analysis accounting for parotid gland volume loss yielded consistent results. These findings support ^{18}F-FDG PET/CT as a potential quantitative biomarker for radiation-induced parotid gland injury and reinforce the clinical rationale for proton therapy when salivary gland preservation is a priority. Whether reduced metabolic injury translates into preserved salivary function and improved patient quality of life remains to be determined. Future prospective multi-institutional studies incorporating standardized imaging protocols, individual parotid dose-volume data, serial imaging time points, and correlation with objective salivary function measures are warranted to validate these findings and inform personalized treatment selection.

Disclosure of conflict of interest

None.

Address correspondence to: Dr. Abass Alavi, Department of Radiology, Hospital of The University of Pennsylvania, 3400 Spruce Street, Philadelphia, PA 19104, USA. Tel: 215-662-3005; Fax: 215-662-7011; E-mail: abass.alavi@pennmedicine.upenn.edu

References

[1] Marur S and Forastiere AA. Head and neck squamous cell carcinoma: update on epidemiology, diagnosis, and treatment. Mayo Clin Proc 2016; 91: 386-396.
[2] Jain S, Takalkar AM and Hall LT. Molecular imaging of head and neck cancers. In: Hall LT, editors. Molecular Imaging and Therapy. Brisbane (AU): 2023.
[3] Alfouzan AF. Radiation therapy in head and neck cancer. Saudi Med J 2021; 42: 247-254.
[4] Rocha PHP, Reali RM, Decnop M, Souza SA, Teixeira LAB, Junior AL, Sarpi MO, Cintra MB, Pinho MC and Garcia MRT. Adverse radiation therapy effects in the treatment of head and neck tumors. Radiographics 2022; 42: 806-821.
[5] Leeman JE, Romesser PB, Zhou Y, McBride S, Riaz N, Sherman E, Cohen MA, Cahlon O and Lee N. Proton therapy for head and neck cancer: expanding the therapeutic window. Lancet Oncol 2017; 18: e254-e265.
[6] Gandhi OH, Lee AE, Gujral J, Ismoilov M, Singh SB, Ghonim M, Ghonim M, Kim MY, Raynor WY, Case MJ, Siddiqi A, Yazdanpanah F, Werner TJ, Saboury B, Revheim ME, Chang YC and Alavi A. Maxillary sinus inflammation assessment using FDG-PET/CT in head and neck cancer patients with photon, proton, and combined radiation therapy. Am J Nucl Med Mol Imaging 2025; 15: 97-104.
[7] Gandhi OH, Shah S, Wittwer E, Gujral J, Al-Daoud O, Moradpour M, Raynor WY, Werner T and Alavi A. Assessment of carotid vasculitis in head and neck cancer patients following individual proton/photon radiation therapy and combined therapy using 18F-FDG PET/CT imaging. J Neurol Surg B Skull Base 2024; 85: S317.
[8] Pinna R, Campus G, Cumbo E, Mura I and Milia E. Xerostomia induced by radiotherapy: an overview of the physiopathology, clinical evidence, and management of the oral damage. Ther Clin Risk Manag 2015; 11: 171-188.
[9] Astaburuaga R, Gabrys HS, Sanchez-Nieto B, Floca RO, Kluter S, Schubert K, Hauswald H and Bangert M. Incorporation of dosimetric gradients and parotid gland migration into xerostomia prediction. Front Oncol 2019; 9: 697.
[10] Amosson CM, Teh BS, Van TJ, Uy N, Huang E, Mai WY, Frolov A, Woo SY, Chiu JK, Carpenter LS, Lu HH, Grant WH 3rd and Butler EB. Dosimetric predictors of xerostomia for head-and-neck cancer patients treated with the smart (simultaneous modulated accelerated radiation therapy) boost technique. Int J Radiat Oncol Biol Phys 2003; 56: 136-144.
[11] van Rijn-Dekker MI, van Luijk P, Schuit E, van der Schaaf A, Langendijk JA and Steenbakkers R. Prediction of radiation-induced parotid gland-related xerostomia in patients with head and neck cancer: regeneration-weighted dose. Int J Radiat Oncol Biol Phys 2023; 117: 750-762.
[12] Zhang M, Gong J, Zhu Y, Yang ZH, Zhou YC, Hu J, Guo H, Li HL, Shi Q, Wang ZF, Liu CH, Su N, Zhao LN, Shi M and Zang J. A predictive model based on the dosimetric parameters of the parotid stem cell region to assess the recovery of radiation-induced xerostomia in long-term survivors of nasopharyngeal carcinoma after radical radiotherapy. Radiother Oncol 2025; 213: 111163.
[13] Zhu A, Lee D and Shim H. Metabolic positron emission tomography imaging in cancer detection and therapy response. Semin Oncol 2011; 38: 55-69.
[14] Basu S, Houseni M and Alavi A. Significance of incidental fluorodeoxyglucose uptake in the parotid glands and its impact on patient management. Nucl Med Commun 2008; 29: 367-373.
[15] Trada Y, Lee MT, Jameson MG, Chlap P, Keall P, Moses D, Lin P and Fowler A. Mid-treatment 18F-FDG PET imaging changes in parotid gland correlates to radiation-induced xerostomia. Radiother Oncol 2023; 186: 109745.
[16] Scheuermann JS, Saffer JR, Karp JS, Levering AM and Siegel BA. Qualification of PET scanners for use in multicenter cancer clinical trials: the American college of radiology imaging network experience. J Nucl Med 2009; 50: 1187-1193.

[17] Sunderland JJ, Boellaard R, Dickson JC, Graves SA and Bailey DL. Standardization of PET/CT performance requirements for whole-body quantitative imaging: an international proposal. J Nucl Med 2025; 66: 1506-1515.
[18] Akamatsu G, Tsutsui Y, Daisaki H, Mitsumoto K, Baba S and Sasaki M. A review of harmonization strategies for quantitative PET. Ann Nucl Med 2023; 37: 71-88.
[19] Vitti ET and Parsons JL. The radiobiological effects of proton beam therapy: impact on DNA damage and repair. Cancers (Basel) 2019; 11: 946.
[20] Tasaka S, Jingu K, Takahashi N, Umezawa R, Yamamoto T, Ishikawa Y, Takeda K, Suzuki Y and Kadoya N. The long-term recovery of parotid glands in nasopharyngeal carcinoma treated by intensity-modulated radiotherapy. Front Oncol 2021; 11: 665837.
[21] Mouminah A, Borja AJ, Hancin EC, Chang YC, Werner TJ, Swisher-McClure S, Korostoff J, Alavi A and Revheim ME. (18)F-FDG-PET/CT in radiation therapy-induced parotid gland inflammation. Eur J Hybrid Imaging 2020; 4: 22.
[22] Roach MC, Turkington TG, Higgins KA, Hawk TC, Hoang JK and Brizel DM. FDG-PET assessment of the effect of head and neck radiotherapy on parotid gland glucose metabolism. Int J Radiat Oncol Biol Phys 2012; 82: 321-326.
[23] Konings AW, Coppes RP and Vissink A. On the mechanism of salivary gland radiosensitivity. Int J Radiat Oncol Biol Phys 2005; 62: 1187-1194.
[24] Avila JL, Grundmann O, Burd R and Limesand KH. Radiation-induced salivary gland dysfunction results from p53-dependent apoptosis. Int J Radiat Oncol Biol Phys 2009; 73: 523-529.
[25] Zlygosteva O, Juvkam IS, Aass HCD, Galtung HK, Soland TM, Malinen E and Edin NFJ. Cytokine levels in saliva are associated with salivary gland fibrosis and hyposalivation in mice after fractionated radiotherapy of the head and neck. Int J Mol Sci 2023; 24: 15218.
[26] Acauan MD, Figueiredo MA, Cherubini K, Gomes AP and Salum FG. Radiotherapy-induced salivary dysfunction: structural changes, pathogenetic mechanisms and therapies. Arch Oral Biol 2015; 60: 1802-1810.
[27] Gunning JA, Gilman KE, Zuniga TM, Simpson RJ and Limesand KH. Parotid glands have a dysregulated immune response following radiation therapy. PLoS One 2024; 19: e0297387.
[28] Schaue D, Kachikwu EL and McBride WH. Cytokines in radiobiological responses: a review. Radiat Res 2012; 178: 505-523.
[29] Zhou L, Zhu J, Liu Y, Zhou PK and Gu Y. Mechanisms of radiation-induced tissue damage and response. MedComm (2020) 2024; 5: e725.
[30] Prasanna PG, Rawojc K, Guha C, Buchsbaum JC, Miszczyk JU and Coleman CN. Normal tissue injury induced by photon and proton therapies: gaps and opportunities. Int J Radiat Oncol Biol Phys 2021; 110: 1325-1340.
[31] Blanchard P, Garden AS, Gunn GB, Rosenthal DI, Morrison WH, Hernandez M, Crutison J, Lee JJ, Ye R, Fuller CD, Mohamed AS, Hutcheson KA, Holliday EB, Thaker NG, Sturgis EM, Kies MS, Zhu XR, Mohan R and Frank SJ. Intensity-modulated proton beam therapy (IMPT) versus intensity-modulated photon therapy (IMRT) for patients with oropharynx cancer - A case matched analysis. Radiother Oncol 2016; 120: 48-55.
[32] Cao J, Zhang X, Jiang B, Chen J, Wang X, Wang L, Sahoo N, Zhu XR, Ye R, Blanchard P, Garden AS, Fuller CD, Gunn GB and Frank SJ. Intensity-modulated proton therapy for oropharyngeal cancer reduces rates of late xerostomia. Radiother Oncol 2021; 160: 32-39.
[33] Wilkie JR, Mierzwa ML, Casper KA, Mayo CS, Schipper MJ, Eisbruch A, Worden FP, El Naqa I, Viglianti BL and Rosen BS. Predicting late radiation-induced xerostomia with parotid gland PET biomarkers and dose metrics. Radiother Oncol 2020; 148: 30-37.
[34] Lodge MA, Chaudhry MA and Wahl RL. Noise considerations for PET quantification using maximum and peak standardized uptake value. J Nucl Med 2012; 53: 1041-1047.
[35] Adams MC, Turkington TG, Wilson JM and Wong TZ. A systematic review of the factors affecting accuracy of SUV measurements. AJR Am J Roentgenol 2010; 195: 310-320.
[36] Burger IA, Huser DM, Burger C, von Schulthess GK and Buck A. Repeatability of FDG quantification in tumor imaging: averaged SUVs are superior to SUVmax. Nucl Med Biol 2012; 39: 666-670.
[37] Cysouw MCF, Golla SVS, Frings V, Smit EF, Hoekstra OS, Kramer GM and Boellaard R; QuIC-ConCePT Consortium. Partial-volume correction in dynamic PET-CT: effect on tumor kinetic parameter estimation and validation of simplified metrics. EJNMMI Res 2019; 9: 12.
[38] Park PSU, Jia L, Raynor WY, Gandhi OH, Park MM, Werner TJ, Hoilund-Carlsen PF and Alavi A. Novel technique of detecting inflammatory and osseous changes in the glenohumeral joint associated with patient age and weight using FDG- and NaF-PET imaging. Am J Nucl Med Mol Imaging 2023; 13: 136-146.
[39] Singh SB, Gandhi OH, Shrestha BB, Glennan P, Bahadur AR, Motamedi N, Khanal K, Wagle S, Hoilund-Carlsen PF, Werner TJ, Revheim ME and Alavi A. [(18)F]NaF PET/CT imaging of iliac bones to assess bone turnover. Mol Imaging Biol 2025; 27: 295-304.
[40] Patil S, Lee W, Patel R, Gerlach A, Patel D, Kata R, Fanta O, Khan T, Jeevika F, Ayubcha C, Gujral J, Gandhi OH, Werner T, Wulff Christensen H, Hoilund-Carlsen PF and Alavi A. Evaluation of physiological bone metabolic activity in the spine with 18F-fluorodeoxyglucose and 18F-sodium fluoride PET: associations with degenerative risk factors. Nucl Med Commun 2026; [Epub ahead of print].
[41] Patil S, Patel D, Lee W, Patel R, Bhave A, Gujral J, Gandhi OH, Jeevika F, Fanta O, Subtirelu R, Werner TJ, Hoilund-Carlsen PF and Alavi A. Determinants of intracranial microcalcification assessed by 18F-sodium fluoride PET. Nucl Med Commun 2026; 47: 588-593.
[42] Ahmed M, Gandhi OH, Singh SB, Gujral J, Park PK, Shrestha BB, Niazi SK, Ismoilov M, Motamedi N, Werner TJ, Revheim ME and Alavi A. Application of [18F]-fluorodeoxyglucose PET/computed tomography to measure volume and metabolic activity of arm muscles. Nucl Med Commun 2025; 46: 1090-1096.
[43] Warwas B, Cremers F, Gerull K, Leichtle A, Bruchhage KL, Hakim SG, Schild SE and Rades D. Risk factors for xerostomia following radiotherapy of head-and-neck cancers. Anticancer Res 2022; 42: 2657-2663.
[44] Castaldi P, Leccisotti L, Bussu F, Micciche F and Rufini V. Role of (18)F-FDG PET-CT in head and neck squamous cell carcinoma. Acta Otorhinolaryngol Ital 2013; 33: 1-8.
[45] Boellaard R, Delgado-Bolton R, Oyen WJ, Giammarile F, Tatsch K, Eschner W, Verzijlbergen FJ, Barrington SF, Pike LC, Weber WA, Stroobants S, Delbeke D, Donohoe KJ, Holbrook S, Graham MM, Testanera G, Hoekstra OS, Zijlstra J,

Visser E, Hoekstra CJ, Pruim J, Willemsen A, Arends B, Kotzerke J, Bockisch A, Beyer T, Chiti A and Krause BJ; European Association of Nuclear Medicine (EANM). FDG PET/CT: EANM procedure guidelines for tumour imaging: version 2.0. Eur J Nucl Med Mol Imaging 2015; 42: 328-354.

[46] Hosono M, Takenaka M, Monzen H, Tamura M, Kudo M and Nishimura Y. Cumulative radiation doses from recurrent PET-CT examinations. Br J Radiol 2021; 94: 20210388.